Geophysical Research Letters

RESEARCH LETTER
10.1029/2022GL097752

Key Points:

- The MJO convection is stronger over the Indian Ocean during La Niña winters than during El Niño winters
- The MJO predictability limit during La Niña winters is enhanced by up to 8 days compared to El Niño winters
- The highest (lowest) predictability limit of the MJO is 39 (31) days during La Niña (El Niño) easterly QBO

Supporting Information:

Supporting Information may be found in the online version of this article.

Correspondence to:

K.-H. Seo,
khseo@pusan.ac.kr

Citation:

Mengist, C. K., & Seo, K.-H. (2022). How long can the MJO be predicted during the combined phases of ENSO and QBO? *Geophysical Research Letters*, *49*, e2022GL097752. https://doi.org/10.1029/2022GL097752

Received 5 JAN 2022
Accepted 9 APR 2022

How Long Can the MJO be Predicted During the Combined Phases of ENSO and QBO?

Chalachew Kindie Mengist[1,2] **and Kyong-Hwan Seo**[1,2,3]

[1]Research Center for Climate Sciences, Pusan National University, Busan, Republic of Korea, [2]BK21 School of Earth and Environmental Systems, Pusan National University, Busan, Republic of Korea, [3]Department of Atmospheric Sciences, Pusan National University, Busan, Republic of Korea

Abstract The predictability limit of the Madden-Julian Oscillation (MJO) in the El Niño and La Niña boreal winters (November-February) is investigated using observational data and historical run outputs of CMIP models. The MJO predictability is computed by the nonlinear local Lyapunov exponents approach for various MJO indices obtained from bandpass-filtered (30–80 days) outgoing longwave radiation, 850-hPa zonal wind, and 200-hPa zonal wind data. The result shows that the MJO predictability during La Niña winters is enhanced by up to 8 days compared to El Niño winters. Enhanced convection of the MJO phases 2–4 with persistence propagation during La Niña winters leads to higher predictability, as compared with those for El Niño winters. The highest (lowest) predictability of the MJO shows 39 (31) days during La Niña/EQBO (El Niño/EQBO) winters. The longer persistence of the MJO during La Niña/EQBO winters leads to higher predictability.

Plain Language Summary The Madden-Julian Oscillation (MJO) is the dominant intraseasonal (30–90 days) variability in the tropical atmosphere and has a great impact on global weather and climate variability. The performance skill of statistical and dynamical models underestimates the upper limit of the MJO prediction. Therefore, we estimate the predictability limit of the MJO during El Niño, La Niña, neutral, and the combined events of El Niño-Southern Oscillation and tropical stratosphere quasi-biennial oscillation (QBO). Observational data and historical run outputs of Coupled Model Intercomparison Project Phase 5 (CMIP5) and Phase 6 (CMIP6) models are used to investigate the MJO predictability limit. The highest predictability limit of 39 days is estimated during the combined phases of La Niña and easterly QBO, when the MJO convection is higher than other events.

1. Introduction

The Madden-Julian Oscillation (MJO; Madden & Julian, 1971, 1972) is the dominant intraseasonal (30–90 days) variability in the tropical atmosphere, and is characterized by eastward propagating (~2–9 m/s), planetary-scale envelops of tropical convection that are tightly coupled with large-scale circulation. The MJO typically originates in the equatorial Indian Ocean (IO), crosses the Maritime Continent (MC), and dies out in the central Pacific. The MJO has a great impact on global weather and climate variability (Zhang, 2013). As the MJO moves eastward, it interacts with tropical weather and climate phenomena, including the monsoon (Lorenz & Hartmann, 2006; Taraphdar et al., 2018; Wheeler et al., 2009), tropical cyclones (Bessafi & Wheeler, 2006; Jiang et al., 2012), and El Niño-Southern Oscillation (ENSO; Hendon et al., 2007; Lee et al., 2019). Through atmospheric teleconnection, the MJO also influences midlatitudes and high latitudes (Lee & Seo, 2019; Seo et al., 2016; Seo & Lee, 2017; Seo & Son, 2012; Stan et al., 2017).

Several studies have investigated the prediction skills (a measure of the accuracy of actual prediction systems) of the MJO during ENSO and quasi-biennial oscillation (QBO). For example, the MJO prediction skill of subseasonal-to-seasonal (S2S) reforecast data ranges from 13 to 35 days during easterly QBO (EQBO) winters and 10–28 days during westerly QBO (WQBO) winters (Lim et al., 2019). Seo (2009) demonstrated that the operational coupled Climate Forecast System (CFS) model of the National Centers for Environmental Prediction (NCEP) has an MJO prediction skill that is influenced by the phase of the ENSO. The MJO prediction skill during the first 2 weeks is slightly higher in neutral and La Niña winters than in El Niño winters (Kim et al., 2018; Seo, 2009). Kim et al. (2018) used the Global Seasonal Forecast System (GloSea) hindcast data and showed that the MJO prediction skill during La Niña winters is up to 25 days and depends on the initial MJO phases. The MJO

prediction skill derived from S2S and GloSea models underestimates the MJO prediction and the forecasting systems still have room for improvement (Ding et al., 2010, 2011; Mengist et al., 2021).

The prediction skill of the MJO during ENSO winters (Kim et al., 2018) and the predictability limit (the skill i.e., predicted with observation data or perfect models) of the MJO during QBO winters (Mengist et al., 2021) have been reported. However, it is unknown whether the MJO is more predictable during El Niño/La Niña winters or during a combined event of El Niño/La Niña and QBO winters. It is also unknown whether ENSO or QBO phases have a greater impact on the MJO predictability limit. Motivated by the above facts, the predictability limit of the MJO during ENSO as well as during combined events of ENSO and QBO winters is evaluated by computing the nonlinear local Lyapunov exponent (NLLE; Chen et al., 2006; Ding et al., 2010, 2011) for multiple MJO indices (Seo et al., 2009). In addition to computing the MJO predictability limit, we address the following questions:

- What are the major differences in the MJO predictability during El Niño and La Niña winters?
- Does the QBO exert similar influence on the MJO propagation during El Niño and La Niña winters?

Mengist et al. (2021) showed that the MJO predictability is sensitive to the choice of the MJO indices. To fill this gap, multiple MJO indices are considered from observational data and historical run outputs of Coupled Model Intercomparison Project Phase 5 (CMIP5) and Phase 6 (CMIP6) models. Details of the NLLE and the MJO indices are described in Section 2. The MJO predictability limit is presented in Section 3. A summary is given in Section 4.

2. Data and Methodology

2.1. Data Set

2.1.1. Observations

Daily averaged outgoing longwave radiation (OLR) data from the National Oceanic and Atmospheric Administration (NOAA) polar-orbiting series of satellites (Liebmann & Smith, 1996) for the period from 1979 to 2018 are used to represent the MJO convection. Zonal winds at 850-hPa (U850) and 200-hPa (U200) are provided by the European Center for Medium-Range Weather Forecasts Re-Analysis Interim data (ERA-Interim; Dee et al., 2011). From the daily OLR and zonal wind data, the MJO index is computed as follows. First, anomaly data are obtained by subtracting the time mean and the first three harmonics of the annual cycle from OLR, U850, and U200 data over the global tropics (15°S–15°N). The resulting anomalies are normalized by the longitudinally averaged variance (Wheeler & Hendon, 2004; Seo et al., 2009), subject to a 30–80-day bandpass Lanczos filter. An empirical orthogonal function (EOF) analysis is then performed to obtain a combined MJO index for an extended boreal winter (November, December, January, and February; NDJF). This MJO index consists of the first two principal components (Wheeler & Hendon, 2004) of the leading combined EOFs (Figure S1 in Supporting Information S1). The variance explained by EOF1 and EOF2 is given at the top right of each panel of Figure S1 in Supporting Information S1, and are significantly separated from the rest of the EOFs (North et al., 1982).

NOAA's Climate Prediction Center classifies an event as El Niño and La Niña winters when the Oceanic Niño Index, which is calculated as the 3-month running mean of the ERSSTv5 SST anomalies in the Niño 3.4 region (120°–170°W, 5°N–5°S; Huang et al., 2017), is above 0.5 °C and below −0.5 °C for a minimum of five consecutive overlapping 3-month periods, respectively. Neutral winters are considered when Niño 3.4 indices are between ±0.5 °C. Details of the list of ENSO years can be found in Table 1.

The QBO index is determined by the mean zonal wind at 50 hPa averaged over 10°S–10°N. Because of the limited data size to estimate the predictability limit of the MJO during the combined events of ENSO and QBO (El Niño/EQBO, El Niño/WQBO, La Niña/EQBO, and La Niña/WQBO winters), we redefined EQBO (WQBO) phases when the NDJF-mean QBO index is smaller (larger) than 0 and an El Niño (La Niña) phases when boreal winter Niño 3.4 indices are positive (negative). Table 1 shows the list of years during the combined events of ENSO and QBO.

2.1.2. CMIP Models

Similar to the observation data, the MJO index is calculated from daily averaged OLR, U850, and zonal wind 250-hPa (U250) historical simulations of CMIP5 (Taylor et al., 2012) and CMIP6 (Eyring et al., 2016) models.

Table 1
List of Years of Observation Data During ENSO and QBO Events

Event (number of winters)	Years
All winter (39)	1980–2018
El Niño (13)	1980^{E}, 1983^{W}, 1987^{N}, 1988^{W}, 1992^{N}, 1995^{N}, 1998^{W}, 2003^{W}, 2005^{W}, 2007^{W}, 2010^{N}, 2015^{E}, 2016^{W}
La Niña (13)	1984^{N}, 1985^{E}, 1989^{W}, 1996^{W}, 1999^{E}, 2000^{W}, 2001^{N}, 2006^{E}, 2008^{E}, 2009^{W}, 2011^{W}, 2012^{N}, 2018^{N}
Neutral ENSO (13)	1981^{W}, 1982^{N}, 1986^{W}, 1990^{E}, 1991^{W}, 1993^{N}, 1994^{W}, 1997^{E}, 2002^{E}, 2004^{E}, 2013^{E}, 2014^{W}, 2017^{W}
El Niño/EQBO (7)	$1980^{E,El}$, 1987^{El}, 1990^{E}, 1992^{El}, 1995^{El}, 2004^{E}, $2015^{E,El}$
El Niño/WQBO (11)	$1983^{W,El}$, $1988^{W,El}$, 1991^{W}, 1993, 1994^{W}, $1998^{W,El}$, $2003^{W,El}$, $2005^{W,El}$, $2007^{W,El}$, 2010^{El}, $2016^{W,El}$
La Niña/EQBO (11)	1982, 1984^{La}, $1985^{E,La}$, 1997^{E}, $1999^{E,La}$, 2001^{La}, 2002^{E}, $2006^{E,La}$, $2008^{E,La}$, 2013^{E}, 2018^{La}
La Niña/WQBO (10)	1981^{W}, 1986^{W}, $1989^{W,La}$, $1996^{W,La}$, $2000^{W,La}$, $2009^{W,La}$, $2011^{W,La}$, 2012^{La}, 2014^{W}, 2017^{W}

Note. $^{W\,(E)}$strong WQBO (EQBO) phase when QBO index is greater (less) than 0.5 (−0.5) standard deviation. ^{N}Neutral phase when absolute QBO index is less than 0.5. $^{El\,(La)}$strong El Niño (La Niña) winter when Niño 3.4 index is above 0.5 (below −0.5)°C. The year 1980 denote 1979–1980 winter.

We selected two models from each, CMIP5 (CNRM-CM5 and CMCC-CMS) and CMIP6 (CNRM-CM6-1 and MPI-ESM1-2-HR), which are capable of representing the observed eastward propagation of the MJO over MC (Ahn et al., 2020). One ensemble member of each model output is used: r1i1p1 for CMIP5 CNRM-CM5 (1953–2005), r1i1p1 for CMIP5 CMCC-CMS (1950–2005), r1i1p1f1 for CMIP6 MPI-ESM1-2-HR (1950–2014), and r1i1p1f2 CMIP6 CNRM-CM6-1 (1950–2014).

2.2. The NLLE Approach

Let an n-dimensional nonlinear dynamical system is governed by

$$\frac{d\mathbf{x}}{dt} = \mathbf{F}(\mathbf{x}) \tag{1}$$

where $\mathbf{x} = [x_1(t),\ x_2(t),\ \ldots,\ x_n(t)]^{\mathrm{T}}$ is the state vector at time t, T is the transpose, and **F**denotes the dynamical system. The evolution of a small error $\boldsymbol{\delta} = [\delta_1(t),\ \delta_2(t),\ \ldots,\ \delta_n(t)]^{\mathrm{T}}$, superimposed on state $\mathbf{x}$, is given by:

$$\frac{d}{dt}\boldsymbol{\delta} = \mathbf{J}(\mathbf{x})\boldsymbol{\delta} + \mathbf{G}(\mathbf{x},\ \boldsymbol{\delta}) \tag{2}$$

where $\mathbf{J}(\mathbf{x})\boldsymbol{\delta}$ represents the tangent linear terms, and $\mathbf{G}(\mathbf{x},\ \boldsymbol{\delta})$ represents the high-order nonlinear terms. Equation 2 could be solved by applying numerical integration along the reference solution $\mathbf{x}$ from $t = t_0$to t_i :

$$\boldsymbol{\delta}\ (t_i) = \boldsymbol{\eta}\left(\mathbf{x}\left(t_0\right), \boldsymbol{\delta}\left(t_0\right), t_i\right) \boldsymbol{\delta}\left(t_0\right) \tag{3}$$

where $\boldsymbol{\eta}\left(\mathbf{x}\left(t_0\right), \boldsymbol{\delta}\left(t_0\right), t_i\right)$ is the nonlinear propagator, which propagates the initial error forward to the error at t_i. The NLLE (Ding et al., 2011) is then defined as:

$$\lambda\left(\mathbf{x}\left(t_0\right), \boldsymbol{\delta}\left(t_0\right), t_i\right) = \frac{1}{t_i - t_0} \ln \frac{\|\boldsymbol{\delta}\ (t_i)\|}{\|\boldsymbol{\delta}(t_0)\|}, \tag{4}$$

here, $\lambda\left(\mathbf{x}\left(t_0\right), \boldsymbol{\delta}\left(t_0\right), t_i\right)$ depends on the initial state $\mathbf{x}\left(t_0\right)$ in phase space, the initial error $\boldsymbol{\delta}\left(t_0\right)$, and time t_i.

The mean relative growth, $\overline{\Phi}$, of the initial error can be obtained as:

$$\overline{\Phi}\left(\boldsymbol{\delta}\left(t_0\right), t_i\right) = \exp\left[\overline{\lambda}\left(\boldsymbol{\delta}\left(t_0\right), t_i\right) t_i\right], \tag{5}$$

here $\overline{\lambda}\left(\boldsymbol{\delta}\left(t_0\right), t_i\right)$ is ensemble-mean NLLE (Ding et al., 2011; Mengist et al., 2021). The method assumes that two state points which have relatively small initial distance will diverge as their trajectories fall into the dynamical system's attractor (Ding & Li, 2007; Hou et al., 2018). Once the mean relative growth, $\overline{\Phi}$, of the initial error reaches the saturation level, all information on the initial state is lost and prediction becomes meaningless (Hou

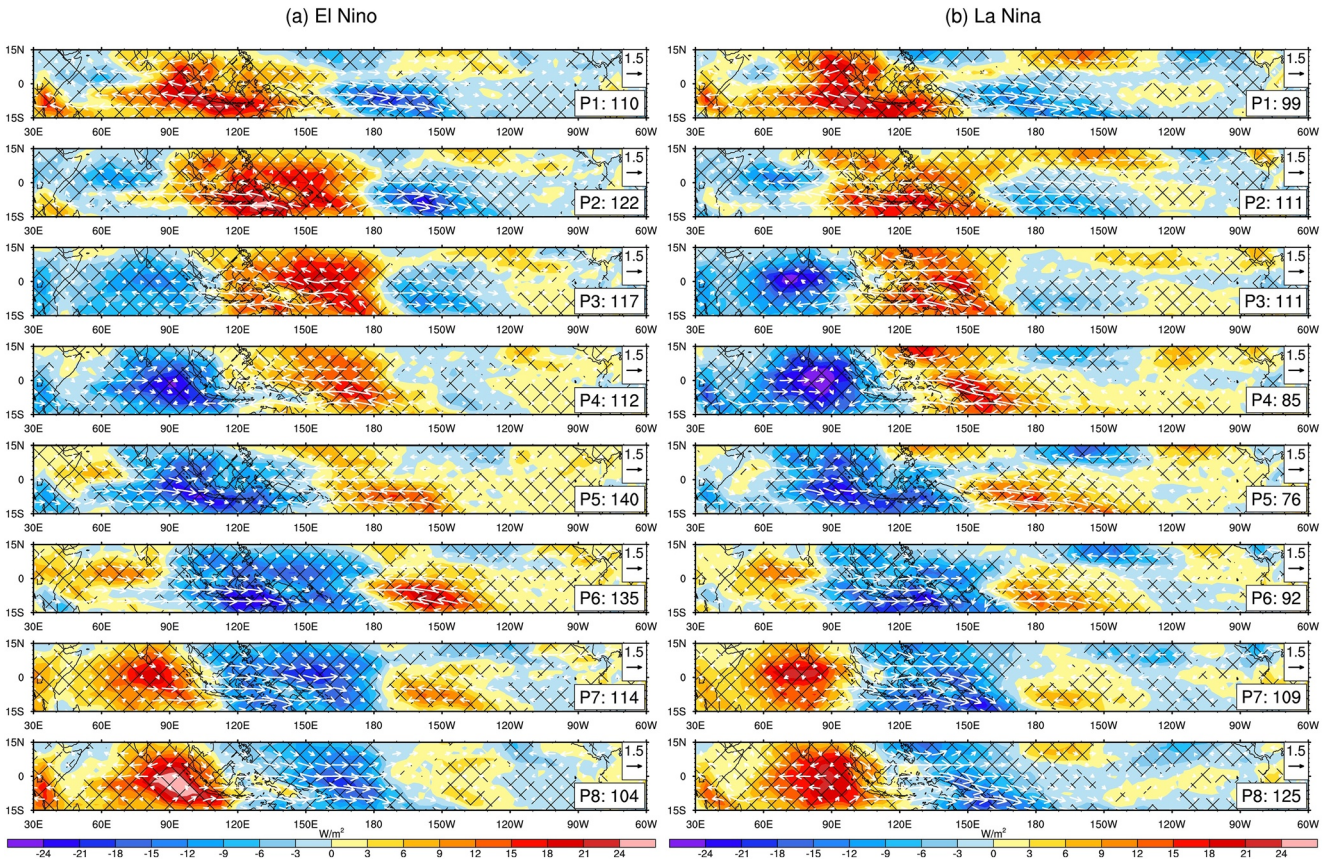

Figure 1. Composite longwave radiation (OLR) (W/m^2; contours) and 850-hPa wind (m/s; arrows) anomalies as a function of the Madden-Julian Oscillation (MJO) phase during (a) El Niño and (b) La Niña winters. The number of days used to create the composite are given at the lower right of each panel. The black stippling indicates that anomalies that are significant at the 0.05 level.

et al., 2018). As a result, the predictability limit is estimated as the time at which 95% of the saturation level is reached (Dalcher & Kalnay, 1987; Ding et al., 2010), to reduce sampling fluctuations.

Finally, the MJO predictability limit is computed for the MJO indices using the NLLE technique during El Niño, La Niña, and neutral winters. Further, the MJO predictability during combined events of ENSO and QBO (El Niño/EQBO, El Niño/WQBO, La Niña/EQBO, and La Niña/WQBO winters) is also calculated.

3. Results

For the amplitude of the MJO index exceeding 1.0, the MJO cycle during El Niño and La Niña boreal winters is divided into eight phases, as shown in Figure 1. The Figure depicts a composite reconstruction of the eastward propagation of the MJO enhanced and suppressed convection and zonal wind of 850-hPa anomalies as a function of the MJO phase. Enhanced convection of phases 2–4 is located in the IO, when easterly winds dominate the east of the deep convection. In this phase, the western Pacific is dominated by suppressed convection anomalies. Propagation of the MJO in phases 2–4 for El Niño winters (Figure 1a) is similar to that of La Niña winters (Figure 1b), with La Niña winters having enhanced convection over IO. For both El Niño and La Niña winters of phases 6–8, the center of deep convection propagates eastward, whereas suppressed convection becomes more prominent over the IO. During these phases, enhanced convection is accompanied by westerly winds. The amplitude of suppressed convection during El Niño winters is stronger than that during La Niña winters.

Figure 2 exhibits the mean error growth for all (black), El Niño (red), La Niña (blue), and neutral (green) winters. The mean error growth shows an exponential increase during the first 2 weeks until reaching a saturation level. Slowly varying boundary conditions, such as external SST forcing, have an effect on the mean error growth

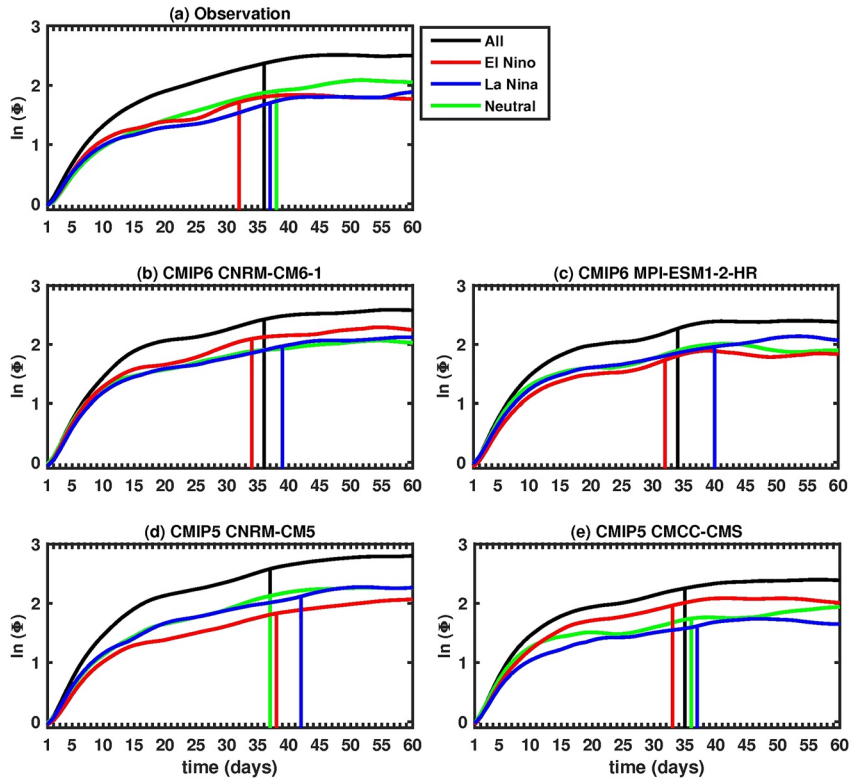

Figure 2. Mean error growth of the Madden-Julian Oscillation (MJO) from (a) observation data and (b–e) Coupled Model Intercomparison Project (CMIP) models for all, El Niño, La Niña, and neutral winters. Vertical lines are days of predictability limit.

after 2 weeks (Seo et al., 2007). The external forcing provided by intraseasonal SST anomalies extends the MJO predictability to a longer time (Ding et al., 2010; Kim et al., 2008). When the error growth reaches a saturation level, all information about the initial states is lost and the prediction becomes meaningless (Ding et al., 2010). The limit of dynamic predictability is quantitatively determined as the time at which the mean error growth reaches 95% of the saturation level (Dalcher & Kalnay, 1987; Ding et al., 2010, 2011; Mengist et al., 2021).

Based on this criterion, the predictability limit of the MJO as shown in Figure 2a is 36, 32, 37, and 38 days for observation in all, El Niño, La Niña, and neutral winters, respectively. The MJO predictability during La Niña winters is 5 days longer than during El Niño winters. According to Li and Ding (2013), the predictability limit can be underestimated when the observation data points are too few to find good local analogs. Because of the short length of observation data sets (each of El Niño, La Niña, and neutral events has 13 winters), the NLLE technique may be unable to find appropriate analogous trajectories. Therefore, a longer data set from historical run outputs of CMIP5 (20 El Niño, 16 La Niña, and 19 neutral winters) and CMIP6 (22 El Niño, 21 La Niña, and 21 neutral winters) are also used in this study to assess the robustness of the results. Figures 2b–2e compare the MJO predictability in CMIP among all, El Niño, La Niña, and neutral winters. As compared with El Niño winters, the predictability limit of the MJO during La Niña winters shows an enhancement of 4 days for CNRM-CM5, 4 days for CMCC-CMS, 4 days for CNRM-CM6-1, and 8 days for MPI-ESM1-2-HR. The predictability limits of the MJO during all and neutral winters are 37 and 38 days for CNRM-CM5; 36 days each for CMCC-CMS; 36 and 39 days for CNRM-CM6-1; and 34 and 32 days for MPI-ESM1-2-HR, respectively. CMIP6 models (CMIP6 INM-CM4 and CMIP6 INM-CM5) that do not exhibit MJO eastward propagation over the MC (Ahn et al., 2020) have equal MJO predictability limits during El Niño and La Niña winters (Figures S2e and S2f in Supporting Information S1). The summary of predictability limit for all data types is given in Table 2, which once again demonstrates that overall, the La Niña and neutral years have greater predictability limit, even in the CMIP5 and 6 model simulations as well as the observed.

Table 2
MJO Predictability Limit (days) During All, El Niño, La Niña, and Neutral Winters

		CMIP6		CMIP5	
Event	Observation	CNRM[a]	MPI[b]	CNRM[c]	CMCC[d]
All	36	36	34	37	35
El Niño	32	34	32	38	33
La Niña	37	39	40	42	37
Neutral	38	39	32	37	36

[a]CNRM-CM6-1. [b]MPI-ESM1-2-HR. [c]CNRM-CM5. [d]CMCC-CMS.

To understand the combined effect of ENSO and QBO on the MJO propagation, observational data are classified into 7 El Niño/EQBO, 11 El Niño/WQBO, 11 La Niña/EQBO, and 10 La Niña/WQBO winters. The background SST anomalies associated with these winters are shown in Figures 3e–3h. Stronger warming (cooling) of SST anomalies over the central and eastern Pacific is observed during WQBO phases of El Niño (La Niña) winters than during EQBO phases. The MJO propagation during the combined phases of ENSO and QBO is shown in Figures 3a–3d. Interestingly, the MJO propagation during El Niño/EQBO (Figure 3a), La Niña/EQBO (Figure 3c), and La Niña/WQBO (Figure 3d) most closely resembles to the fast, slow, and stand MJO types of Wang et al. (2019). On the contrary, the MJO propagation pattern shown in Figure 3b (La Niña/EQBO) less resembles Wang et al. (2019) MJO types. During El Niño/EQBO winters (Figure 3a), an MJO originating from the IO is suppressed over the MC, reinforced over the western Pacific (Sun et al., 2019) and propagates faster toward the central Pacific. Compared with El Niño/EQBO winters, enhanced convection originating from the IO during El Niño/WQBO winters (Figure 3b) is less suppressed over the MC and reinforced over the western Pacific and propagates toward the central Pacific. Reinforcement of the MJO over the western Pacific in Figures 3a and 3b is due to the moisture advection of the El Nino (Figures 3e and 3f) induced positive moisture anomaly from the central Pacific (Sun et al., 2019).

During La Niña winters (Figures 3c and 3d), the effect of the QBO dominates the MJO propagation. So, as shown in Figure 3c, during La Niña/EQBO winters, the strongest MJO convection propagates to the western Pacific without being suppressed over the MC. Figure 3d, on the other hand, shows the enhanced MJO over the IO and barely passes the MC during La Niña/WQBO winters (Sun et al., 2019). Each type of MJO propagation during the four combined events of ENSO and QBO exhibits distinctive characteristics. Therefore, to advance our understanding of the MJO, the predictability limit of the MJO during these four events is estimated.

Figure 3i shows the predictability limit of the MJO for the combined effect of ENSO and QBO. The predictability limit of the MJO during El Niño/EQBO, El Niño/WQBO, La Niña/EQBO, and La Niña/WQBO winters is 31, 34, 39, and 33 days, respectively. The MJO events that are initialized with enhanced convection over the IO survive the damping effect of the MC, tend to propagate persistently toward the western Pacific (Figure 3c), which leads to higher MJO predictability (Figure 3i; Kim et al., 2016). The predictability limit of the MJO during La Niña/EQBO winters is enhanced by 6 days compared with during La Niña/WQBO winters. The predictability limit of the MJO during La Niña winters is dominated by QBO. A decrease in the barrier effect of the MC on the MJO due to a less diurnal cycle of precipitation during La Niña/EQBO winters leads to less suppressed and longer persistence of the MJO than in La Niña/WQBO (Zhang & Zhang, 2018). Compared with La Niña/EQBO (Figure 3c) winters, the MJO during La Niña/WQBO (Figure 3d) winters is suppressed over the IO and disrupted over the MC by Rossby wave-like westward-propagating midlevel dry wind anomalies originating in the central Pacific (DeMott et al., 2018; Feng et al., 2015). EQBO conditions seem to nullify the retarding effect resulting from westward-propagating dry air during La Niña winters, and the MJO is propagating persistently toward the western Pacific. However, the exact physical process needs to be investigated in more detail using a series of sensitivity tests with numerical models. On the other hand, the MJO propagation during El Niño winters over the MC is controlled by El Niño induced downward motion and, due to the reinforcement of the MJO over the western Pacific, the effect of QBO on the MJO is less on the MJO predictability limit (Sun et al., 2019).

4. Conclusions

The NLLE method, which is designed to calculate the limit of predictability for a nonlinear dynamic system (Chen et al., 2006; Ding et al., 2010), was utilized to give a quantitative estimate of the predictability limit of the MJO using the bandpass-filtered (30–80 days) OLR, U850, and U200 (U250) data during El Niño, La Niña, and neutral winters in observational data (1979–2018) and historical run outputs of CMIP5 (1950–2005) and CMIP6 (1950–2014) models. The result shows that the MJO predictability limit during neutral and La Niña winters is higher than in El Niño winters. The MJO predictability during La Niña winters is enhanced by up to 8 days compared to El Niño winters. Enhanced convection of the MJO phases 2–4 with persistence propagation during La Niña winters (Figure 1b) resulted in a higher MJO predictability limit than depressed convection and fast

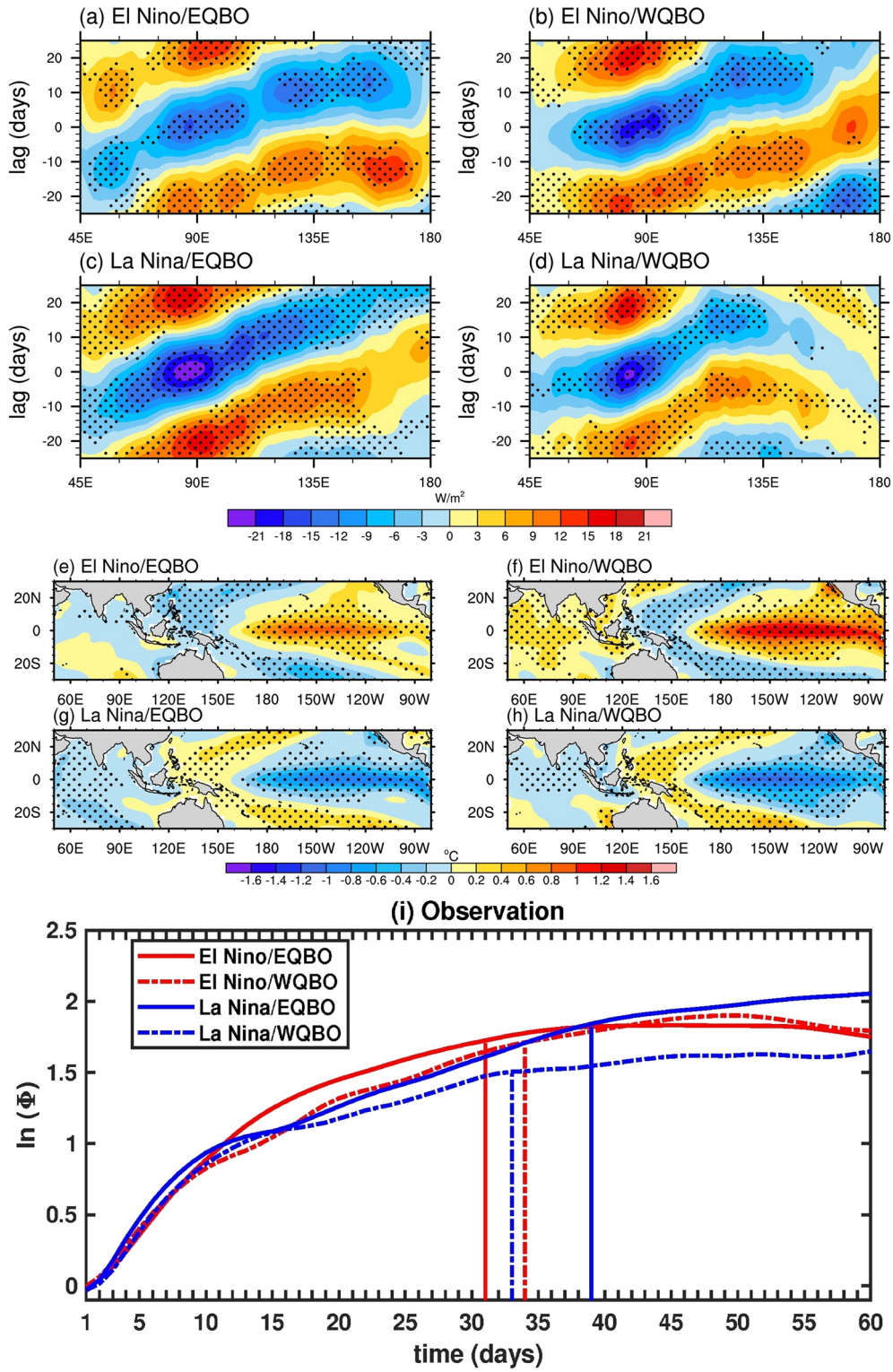

Figure 3. (a–d) Longitude-lag diagrams of equatorially averaged (15°S–15°N) OLR anomalies against OLR at IO (15°S–15°N, 75°–95°E), (e–h) SST anomalies, and (i) mean error growth of MJO during El Niño/EQBO, El Niño/WQBO, La Niña/EQBO, and La Niña/WQBO winters. Anomalies that are significant at the 0.05 level are shown by dots.

propagation during El Niño winters (Kim et al., 2018; Seo, 2009). The higher number of occurrences of strong EQBO events during La Niña winters might also contribute to the higher MJO predictability than during El Niño winters, which have a small number of strong EQBO events. Details of the list of QBO for each ENSO event are given in Table 1.

The MJO predictability during El Niño winters is less affected by the QBO compared with La Niña winters. The MJO suppression over the MC and faster propagation over the western Pacific give less MJO predictability during El Niño/EQBO than during El Niño/WQBO. Enhanced convection and longer persistence of the MJO during La Niña/EQBO winters (Figure 3c) lead to higher predictability as compared with that for La Niña/WQBO winters (Figure 3d).

This study may be used as a benchmark and will help to improve the MJO prediction skills during ENSO and QBO events. The observation data and CMIP models used in this study include internal dynamics and external SST forcing (Seo et al., 2007), so it is difficult to separate their individual contributions to the MJO predictability (Ding et al., 2010). Therefore, the effects of initial conditions and external SST forcing on the MJO's predictability will be studied in the future using more realistic models.

Data Availability Statement

NOAA provides Niño 3.4 index (https://origin.cpc.ncep.noaa.gov/products/analysis_monitoring/ensostuff/ONI_v5.php), ERSSTv5 SST data (https://psl.noaa.gov/data/gridded/data.noaa.ersst.v5.html), OLR data (https://www.esrl.noaa.gov/psd/data/gridded/data.interp_OLR.html), and QBO index (http://www.cpc.ncep.noaa.gov/data/indices/qbo.u50.index). ECMWF provides ERA-Interim data (https://www.ecmwf.int/en/forecasts/datasets/reanalysis-datasets/era-interim). CMIP model data sets are available at ESGF (https://esgf-node.llnl.gov/projects/esgf-llnl).

Acknowledgments
This work was supported by the National Research Foundation of Korea (NRF) grant funded by the Korea government (MSIP; No. NRF-2020R1A2C2009414).

References

Ahn, M., Kim, D., Kang, D., Lee, J., Sperber, K. R., Gleckler, P. J., et al. (2020). MJO propagation across the Maritime continent: Are CMIP6 models better than CMIP5 models? *Geophysical Research Letters*, *47*, e2020GL087250. https://doi.org/10.1029/2020GL087250

Bessafi, M., & Wheeler, M. C. (2006). Modulation of South Indian ocean tropical cyclones by the Madden-Julian oscillation and Convectively coupled equatorial waves. *Monthly Weather Review*, *134*(2), 638–656. https://doi.org/10.1175/MWR3087.1

Chen, B., Li, J., & Ding, R. (2006). Nonlinear local Lyapunov exponent and atmospheric predictability research. *Science in China—Series D: Earth Sciences*, *49*(10), 1111–1120. https://doi.org/10.1007/s11430-006-1111-0

Dalcher, A., & Kalnay, E. (1987). Error growth and predictability in operational ECMWF forecasts. *Tellus A: Dynamic Meteorology and Oceanography*, *39*(5), 474–491. https://doi.org/10.3402/tellusa.v39i5.11774

Dee, D. P., Uppala, S. M., Simmons, A. J., Berrisford, P., Poli, P., Kobayashi, S., et al. (2011). The ERA-Interim reanalysis: Configuration and performance of the data assimilation system. *Quarterly Journal of the Royal Meteorological Society*, *137*(656), 553–597. https://doi.org/10.1002/qj.828

DeMott, C. A., Wolding, B. O., Maloney, E. D., & Randall, D. A. (2018). Atmospheric mechanisms for MJO decay over the Maritime continent. *Journal of Geophysical Research: Atmospheres*, *123*, 5188–5204. https://doi.org/10.1029/2017JD026979

Ding, R., & Li, J. (2007). Nonlinear finite-time Lyapunov exponent and predictability. *Physics Letters A*, *364*(5), 396–400. https://doi.org/10.1016/j.physleta.2006.11.094

Ding, R., Li, J., & Seo, K.-H. (2010). Predictability of the Madden-Julian oscillation estimated using observational data. *Monthly Weather Review*, *138*(3), 1004–1013. https://doi.org/10.1175/2009MWR3082.1

Ding, R., Li, J., & Seo, K.-H. (2011). Estimate of the predictability of boreal summer and winter intraseasonal oscillations from observations. *Monthly Weather Review*, *139*(8), 2421–2438. https://doi.org/10.1175/2011MWR3571.1

Eyring, V., Bony, S., Meehl, G. A., Senior, C. A., Stevens, B., Stouffer, R. J., & Taylor, K. E. (2016). Overview of the coupled model Intercomparison Project phase 6 (CMIP6) experimental design and organization. *Geoscientific Model Development*, *9*(5), 1937–1958. https://doi.org/10.5194/gmd-9-1937-2016

Feng, J., Li, T., & Zhu, W. (2015). Propagating and nonpropagating MJO events over Maritime continent. *Journal of Climate*, *28*(21), 8430–8449. https://doi.org/10.1175/JCLI-D-15-0085.1

Hendon, H. H., Wheeler, M. C., & Zhang, C. (2007). Seasonal dependence of the MJO-ENSO relationship. *Journal of Climate*, *20*(3), 531–543. https://doi.org/10.1175/JCLI4003.1

Hou, Z., Li, J., Ding, R., Karamperidou, C., Duan, W., Liu, T., & Feng, J. (2018). Asymmetry of the predictability limit of the warm ENSO phase. *Geophysical Research Letters*, *45*, 7646–7653. https://doi.org/10.1029/2018GL077880

Huang, B., Thorne, P. W., Banzon, V. F., Boyer, T., Chepurin, G., Lawrimore, J. H., et al. (2017). Extended reconstructed sea surface temperature, Version 5 (ERSSTv5): Upgrades, validations, and intercomparisons. *Journal of Climate*, *30*(20), 8179–8205. https://doi.org/10.1175/JCLI-D-16-0836.1

Jiang, X., Zhao, M., & Waliser, D. E. (2012). Modulation of tropical cyclones over the eastern Pacific by the intraseasonal variability simulated in an AGCM. *Journal of Climate*, *25*(19), 6524–6538. https://doi.org/10.1175/JCLI-D-11-00531.1

Kim, H., Lee, M.-I., Kim, D., Kang, H.-S., & Hyun, Y.-K. (2018). Representation of boreal winter MJO and its teleconnection in a dynamical ensemble seasonal prediction system. *Journal of Climate*, *31*(21), 8803–8818. https://doi.org/10.1175/JCLI-D-18-0039.1

Kim, H.-M., Hoyos, C. D., Webster, P. J., & Kang, I.-S. (2008). Sensitivity of MJO simulation and predictability to sea surface temperature variability. *Journal of Climate*, *21*(20), 5304–5317. https://doi.org/10.1175/2008JCLI2078.1

Kim, H.-M., Kim, D., Vitart, F., Toma, V. E., Kug, J.-S., & Webster, P. J. (2016). MJO propagation across the Maritime continent in the ECMWF ensemble prediction system. *Journal of Climate*, *29*(11), 3973–3988. https://doi.org/10.1175/JCLI-D-15-0862.1

Lee, H.-J., & Seo, K.-H. (2019). Impact of the Madden-Julian oscillation on Antarctic sea ice and its dynamical mechanism. *Scientific Reports*, *9*(1), 10761. https://doi.org/10.1038/s41598-019-47150-3

Lee, R. W., Woolnough, S. J., Charlton-Perez, A. J., & Vitart, F. (2019). ENSO modulation of MJO teleconnections to the North Atlantic and Europe. *Geophysical Research Letters*, *46*, 13535–13545. https://doi.org/10.1029/2019GL084683

Li, J., & Ding, R. (2013). Temporal-spatial distribution of the predictability limit of monthly sea surface temperature in the global oceans: Distribution of the predictability limit of monthly SST. *International Journal of Climatology*, *33*(8), 1936–1947. https://doi.org/10.1002/joc.3562

Liebmann, B., & Smith, C. A. (1996). Description of a complete (interpolated) outgoing longwave radiation dataset. *Bulletin of the American Meteorological Society*, *77*(6), 1275–1277.

Lim, Y., Son, S.-W., Marshall, A. G., Hendon, H. H., & Seo, K.-H. (2019). Influence of the QBO on MJO prediction skill in the subseasonal-to-seasonal prediction models. *Climate Dynamics*, *53*(3), 1681–1695. https://doi.org/10.1007/s00382-019-04719-y

Lorenz, D. J., & Hartmann, D. L. (2006). The effect of the MJO on the North American monsoon. *Journal of Climate*, *19*(3), 333–343. https://doi.org/10.1175/JCLI3684.1

Madden, R. A., & Julian, P. R. (1971). Detection of a 40–50 Day oscillation in the zonal wind in the tropical Pacific. *Journal of the Atmospheric Sciences*, *28*(5), 702–708. https://doi.org/10.1175/1520-0469(1971)028<0702:DOADOI>2.0.CO;2

Madden, R. A., & Julian, P. R. (1972). Description of global-scale circulation cells in the tropics with a 40–50 Day period. *Journal of the Atmospheric Sciences*, *29*(6), 1109–1123. https://doi.org/10.1175/1520-0469(1972)029<1109:DOGSCC>2.0.CO;2

Mengist, C. K., Seo, K.-H., Ding, R., & Son, S.-W. (2021). Potential predictability of the MJO during easterly and westerly phases of the QBO. *Climate Dynamics*, *57*(3–4), 717–726. https://doi.org/10.1007/s00382-021-05733-9

North, G. R., Bell, T. L., Cahalan, R. F., & Moeng, F. J. (1982). Sampling errors in the estimation of empirical orthogonal functions. *Monthly Weather Review*, *110*(7), 699–706. https://doi.org/10.1175/1520-0493(1982)110<0699:SEITEO>2.0.CO;2

Seo, K.-H. (2009). Statistical-dynamical prediction of the Madden-Julian oscillation using NCEP climate Forecast system (CFS). *International Journal of Climatology*, *29*(14), 2146–2155. https://doi.org/10.1002/joc.1845

Seo, K.-H., & Lee, H.-J. (2017). Mechanisms for a PNA-like teleconnection pattern in response to the MJO. *Journal of the Atmospheric Sciences*, *74*(6), 1767–1781. https://doi.org/10.1175/JAS-D-16-0343.1

Seo, K.-H., Lee, H.-J., & Frierson, D. M. W. (2016). Unraveling the teleconnection mechanisms that induce wintertime temperature anomalies over the Northern Hemisphere continents in response to the MJO. *Journal of the Atmospheric Sciences*, *73*(9), 3557–3571. https://doi.org/10.1175/JAS-D-16-0036.1

Seo, K.-H., Schemm, J.-K. E., Wang, W., & Kumar, A. (2007). The boreal summer intraseasonal oscillation simulated in the NCEP climate Forecast system: The effect of sea surface temperature. *Monthly Weather Review*, *135*(5), 1807–1827. https://doi.org/10.1175/MWR3369.1

Seo, K.-H., & Son, S.-W. (2012). The global atmospheric circulation response to tropical diabatic heating associated with the Madden-Julian oscillation during Northern winter. *Journal of the Atmospheric Sciences*, *69*(1), 79–96. https://doi.org/10.1175/2011JAS3686.1

Seo, K.-H., Wang, W., Gottschalck, J., Zhang, Q., Schemm, J.-K. E., Higgins, W. R., & Kumar, A. (2009). Evaluation of MJO Forecast skill from Several statistical and dynamical Forecast models. *Journal of Climate*, *22*(9), 2372–2388. https://doi.org/10.1175/2008JCLI2421.1

Stan, C., Straus, D. M., Frederiksen, J. S., Lin, H., Maloney, E. D., & Schumacher, C. (2017). Review of tropical-extratropical teleconnections on intraseasonal time scales. *Reviews of Geophysics*, *55*, 902–937. https://doi.org/10.1002/2016RG000538

Sun, L., Wang, H., & Liu, F. (2019). Combined effect of the QBO and ENSO on the MJO. *Atmospheric and Oceanic Science Letters*, *12*(3), 170–176. https://doi.org/10.1080/16742834.2019.1588064

Taraphdar, S., Zhang, F., Leung, L. R., Chen, X., & Pauluis, O. M. (2018). MJO affects the monsoon onset timing over the Indian region. *Geophysical Research Letters*, *45*, 10011–10018. https://doi.org/10.1029/2018GL078804

Taylor, K. E., Stouffer, R. J., & Meehl, G. A. (2012). An overview of CMIP5 and the experiment design. *Bulletin of the American Meteorological Society*, *93*(4), 485–498. https://doi.org/10.1175/BAMS-D-11-00094.1

Wang, B., Chen, G., & Liu, F. (2019). Diversity of the Madden-Julian oscillation. *Science Advances*, *5*(7), eaax0220. https://doi.org/10.1126/sciadv.aax0220

Wheeler, M. C., & Hendon, H. H. (2004). An all-season real-time multivariate MJO index: Development of an index for monitoring and prediction. *Monthly Weather Review*, *132*(8), 1917–1932. https://doi.org/10.1175/1520-0493(2004)132<1917:AARMMI>2.0.CO;2

Wheeler, M. C., Hendon, H. H., Cleland, S., Meinke, H., & Donald, A. (2009). Impacts of the Madden-Julian oscillation on Australian rainfall and circulation. *Journal of Climate*, *22*(6), 1482–1498. https://doi.org/10.1175/2008JCLI2595.1

Zhang, C. (2013). Madden-Julian oscillation: Bridging weather and climate. *Bulletin of the American Meteorological Society*, *94*(12), 1849–1870. https://doi.org/10.1175/BAMS-D-12-00026.1

Zhang, C., & Zhang, B. (2018). QBO-MJO connection. *Journal of Geophysical Research: Atmospheres*, *123*, 2957–2967. https://doi.org/10.1002/2017JD028171